PAPER

Check for updates

Creating water-in-salt-like environment using coordinating anions in non-concentrated aqueous electrolytes for efficient Zn batteries†

Dario Gomez Vazquez, [a] Travis P. Pollard, [b] Julian Mars,[c] Ji Mun Yoo,[a] Hans-Georg Steinrück, [d] Sharon E. Bone,[e] Olga V. Safonova, [f] Michael F. Toney, [cg] Oleg Borodin[b] and Maria R. Lukatskaya ⋆[a]

Rechargeable aqueous Zn metal batteries are promising systems for grid storage because of their high energy density, low cost, and non-flammability. However, Zn metal anodes have major limitations due to dendrite formation and concurrent water splitting during charge–discharge cycling. Both processes negatively affect coulombic efficiency (CE) and long-term cycling stability. Water-in-salt (WIS) electrolytes were previously proposed to address these challenges, yielding improvements in the cycling stability of Zn metal anodes. While WIS electrolytes help increase CE, they require high amounts of salt (often toxic) and have dramatically increased viscosity, which in turn limit their transport properties, charge–discharge rates, and usability in advanced Zn batteries. In this manuscript, we propose a strategy for simultaneously achieving high CE ($>99\%$), high rate, low cost and reduced environmental footprint. Specifically, we show that by using coordinating anions like acetate a WIS-like Zn coordination environment can be achieved even in relatively dilute conditions, enabling prolonged cycling of Zn metal anodes. Such electrolytes have an order of magnitude higher conductivity and lower viscosity than traditional WIS electrolytes, thus enabling lower overpotentials and higher rate of Zn plating/stripping.

Introduction

Increasing the utilization of renewable energy sources such as wind and solar is necessary to reduce carbon emissions to the atmosphere.[1,2] However, due to the intermittent nature of these energy sources, it is critical to develop low-cost, safe, and reliable grid-level energy storage.[3–5] While Li-ion batteries are a mature technology, concerns over the usage of flammable electrolytes, their relatively high cost as well as projected supply shortages for Li[6] make them suboptimal for grid storage.[7]

[a] *Department of Mechanical and Process Engineering, ETH Zurich, 8092 Zurich, Switzerland. E-mail: mlukatskaya@ethz.ch*

[b] *Battery Science Branch, DEVCOM Army Research Laboratory, Adelphi, MD, 20783, USA*

[c] *Department of Chemical and Biological Engineering, University of Colorado Boulder, Boulder, CO, 80309, USA*

[d] *Department Chemie, Universität Paderborn, Paderborn, Germany*

[e] *Stanford Synchrotron Radiation Lightsource, SLAC National Accelerator Laboratory, Menlo Park, CA, 94025, USA*

[f] *Paul Scherrer Institute, Villigen PSI, 5232, Switzerland*

[g] *Renewable and Sustainable Energy Institute, University of Colorado Boulder, Boulder, CO, 80309, USA*

Rechargeable aqueous batteries offer a promising alternative for grid energy storage due to their lower cost and improved safety enabled by the use of non-flammable and environmentally benign electrolytes.[8,9] Among these, Zn metal batteries are of great interest due to the high theoretical gravimetric ($\sim$820 mA h g^{-1}) and volumetric ($\sim$5800 mA h cm^{-3}) capacities of Zn metal anodes as well as the high abundance, mature recycling infrastructure and low toxicity of Zn.[10–12] However, the commercialization of Zn metal anodes faces several critical challenges. First, concurrent hydrogen evolution reaction (HER) during Zn plating negatively affects coulombic efficiency (CE) and leading to continuous electrolyte consumption and pressure-build-up in a battery cell, thereby reducing cycling stability.[10,11,13–15] Another major problem for Zn metal anodes is dendrite formation during plating that can lead to short-circuiting of the cells.[16,17]

Several approaches involving electrolyte engineering were proposed to address these challenges.[15–20] For example, the replacement of relatively dilute, salt-in-water electrolytes with highly concentrated ones (water-in-salt electrolytes, WIS) was shown effective in suppressing both HER and dendrite formation.[21–23] In WIS electrolytes, the fraction of salts is higher than water by weight and/or volume.[24] As a result, at such high

1982 | *Energy Environ. Sci.*, 2023, **16**, 1982–1991

This journal is © The Royal Society of Chemistry 2023

salt concentrations, there are not enough water molecules to fully solvate ions of the electrolyte, leading to disruption of hydrogen bonding and increased ion–ion interactions (ion pair and ion aggregate formation). This leads to increased participation of anions in Zn-ion solvation[22,25] that together with disrupted hydrogen bonding is assumed to suppress HER, yielding improved coulombic efficiencies and cycle life.[26,27] For example, the use of 1 m $ZnTFSI_2$ + 20 m LiTFSI WIS or 30 m K acetate (KOAc) + 3 m Li acetate (LiOAc) + 3 m Zn acetate ($ZnOAc_2$) electrolytes leads to an increase in Zn plating-stripping CE up to 99.9%[22] and 99.6%,[28] respectively, compared to single salt dilute electrolytes.

In this work, we examine whether the WIS regime for electrolytes is always the most advantageous for cycling Zn anodes or if equivalent or even more promising performance can be achieved with non-WIS electrolytes. Prior research indicates that Zn plating and stripping efficiency is strongly affected by the Zn-ion coordination environment that is influenced by electrolyte speciation.[14,29] However, the primary parameter considered in much of the literature relates to electrolyte concentration, where at WIS conditions anions are forced into coordination sphere of Zn. Meanwhile, it is known that anion-rich, water-deficient coordination can be achieved for cations even in salt-in-water solutions if anion coordination ability is higher than that of water.[30–32] Herein, we investigate how electrolyte concentration affects the local coordination of Zn ions in mixed-cation acetate solutions and how modified electrolyte speciation affects the physicochemical characteristics of electrolytes and the Zn plating/stripping efficiency. Acetate salts were chosen due to the acetate anion's strong coordination ability towards transition metal ions (relative to water), their low cost, and environmental friendliness.[33–35] We show that the use of WIS systems *per se* does not necessarily increase the efficiency of Zn batteries and that the role of the anion and supporting cation should be considered in electrolyte engineering for Zn batteries. For the examined solution series ($Zn_{0.2}K_{0.8}OAc_{1.2}$ nH_2O), we demonstrate that a WIS-like coordination environment is already observed around Zn for a water-to-cation ratio of $n = 10$, allowing us to achieve both high CE (99.8%), rate performance compared to both more dilute or concentrated (WIS) regimes. Importantly, we provide comprehensive electrolyte characterization linking its structure and physicochemical properties to electrochemical performance. In addition to extensive validation of the modeling results, we uncover and discuss quantitative differences with the previous reports for WIS bisalt Zn aqueous acetate-based electrolytes.[36]

Results and discussion

Zn-ion solvation, electrolyte structure, and physicochemical properties

Achieving the WIS regime for Zn^{2+}-based electrolytes is challenging due to insufficient solubility of most Zn salts and often
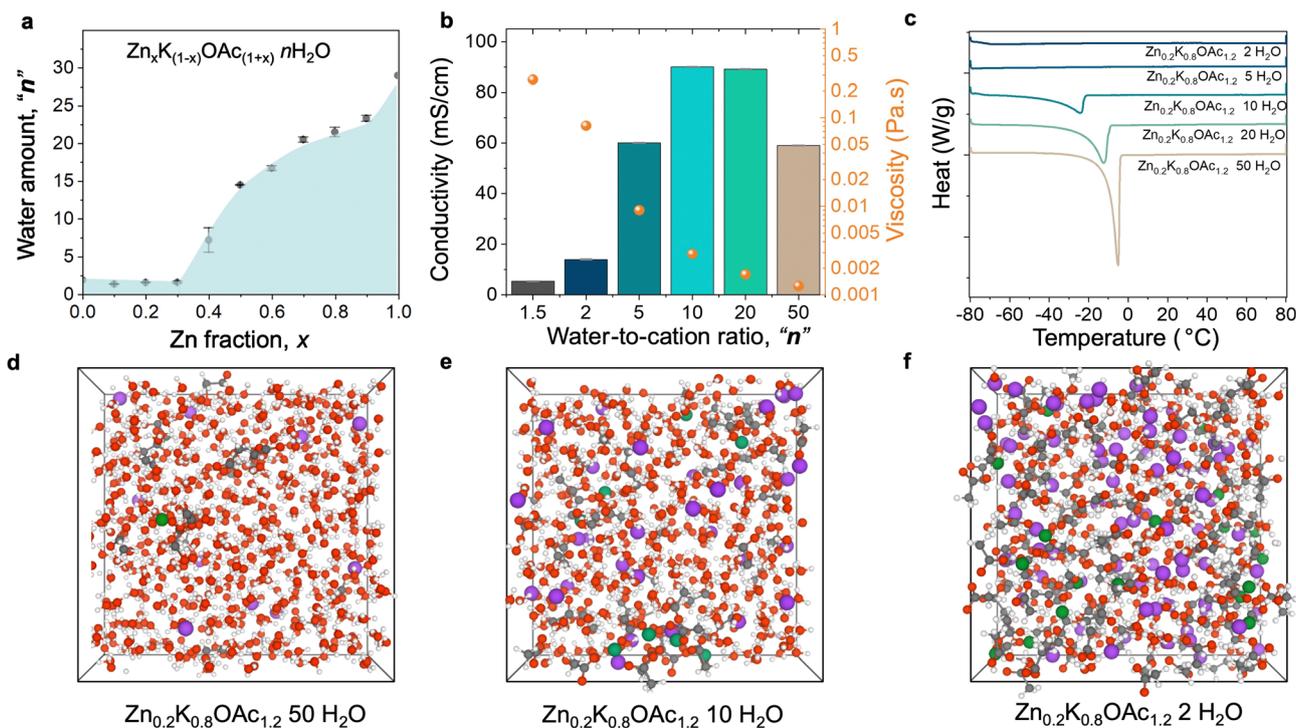

Fig. 1 Physicochemical properties of Zn–K acetate solutions at room temperature. (a) Measured liquidus line of the $Zn_xK_{(1-x)}OAc_{(1+x)}$ salt–water mixtures. (b) Conductivity and viscosity as a function of water-to-cation ratio n (c) Differential scanning calorimetry data or various water-to-cation ratio n. (d)–(f) Molecular dynamics simulation boxes (for visualization) for the electrolytes $Zn_{0.2}K_{0.8}OAc_{1.2}$ nH_2O with $n = 50$ (d), 10 (e), and 2 (f). Color scheme: Zn – green, K – purple, O – red, H – white, and C – gray.

This journal is © The Royal Society of Chemistry 2023

Energy Environ. Sci., 2023, **16**, 1982–1991 | **1983**

requires the use of a supporting salt. In this work, we study environmentally friendly zinc and potassium acetate electrolytes, where potassium acetate is a supporting salt that enables WIS conditions.[33] First, we evaluated the solubility of Zn and K acetate (OAc) mixtures $Zn_xK_{1-x}OAc_{1+x}$ nH_2O, where "x" is a molar fraction of Zn salt and "n" is the number of water molecules per cation (Zn^{2+} and K^+). The measured liquidus line (Fig. 1(a)) shows that the maximum solubility is achieved when the Zn fraction is 0.1–0.3, which corresponds to a WIS electrolyte (1.5 water molecules per cation). Because we observe a dramatic increase in viscosity for $x = 0.3$ that negatively affects ion transport (Fig. S1a, ESI†), we select the composition series with $x = 0.2$ ($Zn_{0.2}K_{0.8}OAc_{1.2}$ nH_2O, with n varying from 1.5 (WIS) to 50 (relatively dilute)).

Table S1 (ESI†) summarizes the physicochemical properties of the $Zn_{0.2}K_{0.8}OAc_{1.2}$ nH_2O electrolytes. The presence of K^+ results in an increased conductivity of the electrolyte compared to pure $Zn(OAc)_2$ (Table S1, ESI†). Conductivity of mixed-cation electrolytes reaches a maximum of 90 mS cm^{-1} at $n = 10$ (Fig. 1(b)). When the electrolyte enters WIS regime ($n < 5$), conductivity rapidly decreases while viscosity dramatically increases, reaching a maximum at $n = 1.5$ (lowest value tested). The Walden plot analysis shows that the behavior of studied

Zn–K acetate electrolyte series can be characterized as "good ionic" or moderately "associated"[37] (Fig. S1b, ESI†). Further, we analyzed thermal properties of the solution series using differential scanning calorimetry (DCS). Fig. 1(c) depicts the corresponding differential scanning thermograms. The most dilute electrolyte ($n = 50$) displays normal melting/freezing at temperatures −4.9 °C. Upon increasing the electrolyte concentration from $n = 50$ to $n = 10$, the melting drops to −24 °C at $n = 10$. Further increases in electrolyte concentration ($n \leq 5$) are characterized by the suppression of the electrolyte melting/freezing transition and drop in heat capacities (Fig. S2, ESI†). Similar behavior was observed for Li-KOAc[33] and other[38–41] WIS electrolytes.

Next, we studied the changes in electrolyte structure and speciation (MD generated electrolyte visualization, Fig. 1(d)–(f)). From pair distribution function (PDF) measurements (Fig. 2(a)) we observe that a concentration increase leads to an increase in ion pair formation between Zn^{2+} and OAc$^-$ as signified by increased intensity of the peak at ∼3.6 Å (Zn–C). This is also in agreement with molecular dynamics (MD) simulations results (see the radial distribution function (RDF) analysis, Fig. S3, ESI†). Similarly, ^{13}C NMR data shows upfield shift of the carbon of carboxylate group (acetate anion) with concentration
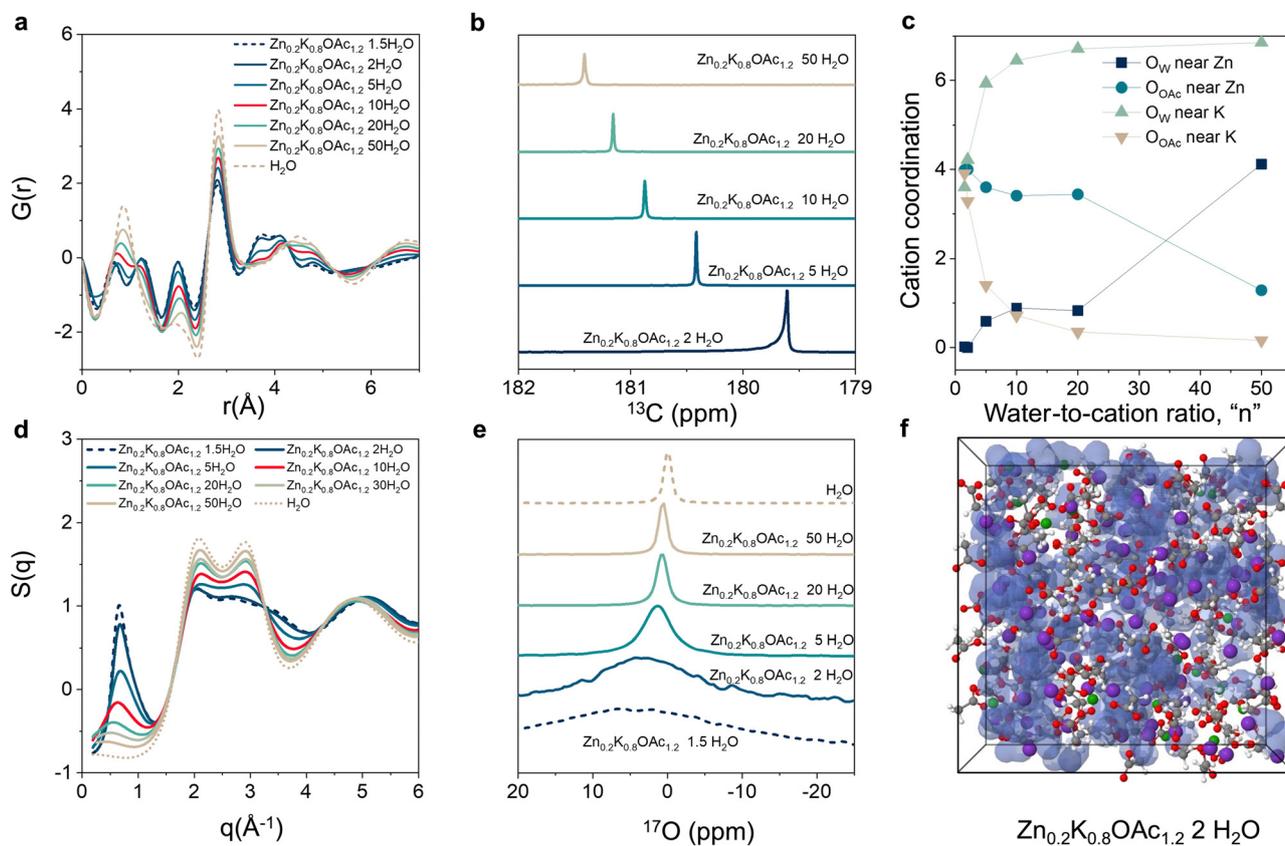

Fig. 2 Solution structure and speciation of the $Zn_{0.2}K_{0.8}OAc_{1.2}$ nH_2O electrolyte series. (a) X-ray total scattering-derived total molecular pair distribution function (PDF). (b) ^{13}C NMR of the carboxylic carbon in acetate anion. (c) MD predicted coordination environment of Zn (within 2.5 Å) and K (within 3.6 Å) cations as a function of electrolyte concentration. (d) X-Ray scattering structure factor $S(q)$. (e) ^{17}O NMR spectra of the water "region". (f) MD simulation box for the $Zn_{0.2}K_{0.8}OAc_{1.2}$ $2H_2O$ visualizing water domains (blue). Color scheme: water domains (blue), Zn – green, K – purple, O – red, H – white, and C – gray.

1984 | Energy Environ. Sci., 2023, 16, 1982–1991

This journal is © The Royal Society of Chemistry 2023

(Fig. 2(b)) as a result of ion shielding due to increased number of OAc[−] coordinating to the same cation.[42]

MD simulations show that K^{+} has stronger affinity to water vs acetate while the reverse is true for Zn^{2+}. Even in dilute conditions ($n = 50$), simulations suggest Zn^{2+} is already partially coordinated by acetate while K^{+} is fully coordinated by water (Fig. 2(c)). Starting from intermediate concentrations ($n = 10$), Zn^{2+} becomes mainly coordinated by acetate while K^{+} remains coordinated mostly by water molecules (Fig. 2(c) and Fig. S4, ESI†). Upon further increase in concentration ($n \leq 5$) the electrolyte enters the WIS regime and K^{+} starts to be partially coordinated by acetate (Fig. 2(c)). Changes in electrolyte structure at the nanoscale are reflected in the X-ray scattering data $S(q)$. As concentration increases, a progressive increase in the intensity of the low-q peak ($0.3\ \text{Å}^{-1} < q < 1.5\ \text{Å}^{-1}$), as well as its shift towards larger q values, is observed (Fig. 2(d)).[43] This peak can be attributed to the nanoscale compositional segregation.[34] It is important to note that experimental and MD-calculated structure factors, $S(q)$, are in good agreement with each other (Fig. S5–S7, ESI†), indicating sufficient accuracy of the MD predictions.

We also observe that the increase in concentration results in a disruption of the hydrogen bonding network and decreases the prevalence of "free" water.^{17}O NMR shows increased interaction of the water molecules with cations in WIS regime ($n = 2$) as can be seen from the peak shift by 4 ppm compared to pure water (Fig. 2(e)).[33] Moreover, MD simulations indicate

formation of the water-rich and water-deficient domain at $n < 10$ (Fig. 2(f) and Fig. S8a–c, ESI†).

Zn^{2+} solvation environment

The coordination environment of Zn^{2+} was studied using XAS (Fig. 3(a)). X-ray absorption near-edge structure (XANES) of Zn^{2+} shows a gradual decrease in the edge energy with increasing concentration (Fig. 3(b)). We speculate that this can be explained by the increased electron density on Zn^{2+} when water molecules are displaced by acetate anions in the solvation shell (acetate anion has a higher Lewis basicity than water[30,44,45]). This explanation also agrees with the ^{13}C NMR results (discussed above, Fig. 2(b)) and MD-generated RDF (Fig. 2(c) and Fig. S4, ESI†) where the acetate interactions with cations and RDF peak for Zn–O_{OAc} relative to Zn–O_W increase with concentration.

Next, evolution of the Zn^{2+} coordination environment in electrolytes as a function of concentration was examined using extended X-ray absorption fine structure (EXAFS). All studied electrolytes display a prominent peak at $\sim 1.5\ \text{Å}$ that can be attributed to Zn–O (Fig. 3(c)). Increasing concentration leads to an increasing intensity in the peak shoulder at $\sim 2.5\ \text{Å}$ and the peak at 3–4 Å indicative of a change in the Zn^{2+} coordination environment. As NMR, PDF, and XANES data suggest, the displacement of water from the coordination sphere of Zn^{2+} takes place when concentration is increased. The presence of isosbestic points in the EXAFS spectra indicates co-existence of
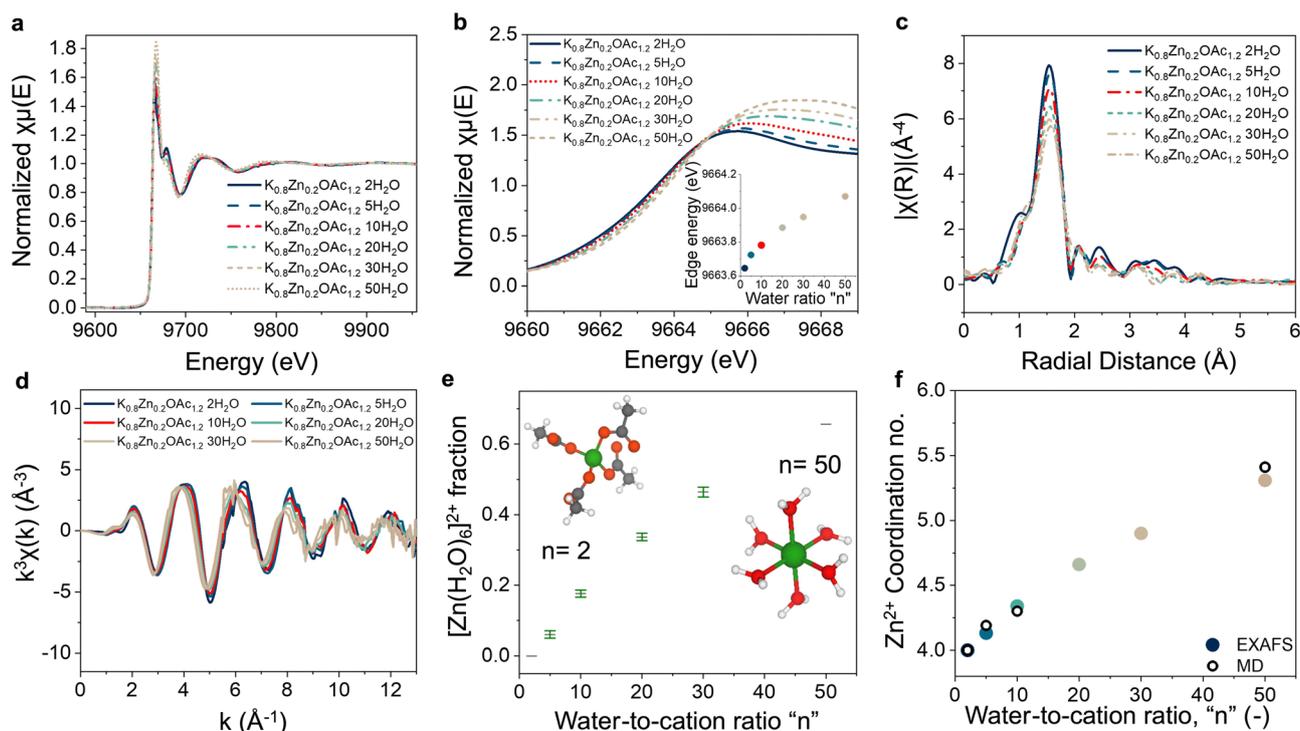

Fig. 3 XAS results analysis for the electrolytes $Zn_{0.2}K_{0.8}OAc_{1.2}\ nH_2O$ as a function of n. (a) Normalized XAS spectra. (b) Normalized XANES region and edge energy (inset) $^\circ E$. (c) EXAFS changes in radial space (d) EXAFS changes in k space. (e) Zn^{2+} coordination environment extracted from EXAFS fittings. Y axis shows the fraction, x, of Zn^{2+} coordinated by water ($[Zn(H_2O)_6]^{2+}$) and ($1 − x$) of Zn coordinated by acetate ($[Zn(OAc)_4]^{2−}$). (f) Zn^{2+} coordination number as calculated from MD $vs.$ values obtained from linear combination fitting of the EAXFS.

This journal is © The Royal Society of Chemistry 2023

Energy Environ. Sci., 2023, **16**, 1982–1991 | **1985**

two coordination environments of Zn^{2+} in each electrolyte of the series, from dilute ($n = 50$) to the most concentrated ($n = 2$) (Fig. S9a, ESI†). As a result, for each electrolyte in the series, we can generate high quality fitting of the EXAFS spectra using a linear combination of the experimental spectra of most diluted ($n = 50$) and most concentrated electrolytes ($n = 2$) (Fig. S9b–f, ESI†).

To obtain a more quantitative understanding of the Zn coordination environment at different concentrations, we compared the quality of fits of the EXAFS spectra for the electrolytes with density functional theory (DFT) generated Zn^{2+} coordination models (Table S2, ESI†). In dilute conditions, the best fit was obtained using a linear combination of the two DFT models, $[Zn(H_2O)_6]^{2+}$ and $[Zn(OAc)_4]^{2-}$ with respective fractions of 0.66 and 0.34 (Fig. S10a–c, ESI†), which improved the goodness of fit (Tables S2 and S3, ESI†). These results are also in agreement with MD simulations that suggest co-presence of acetate and water molecules in the coordination sphere of Zn^{2+} in dilute conditions ($n = 50$) (Fig. 2(c)). For the most concentrated electrolyte ($n = 2$), the best fit was generated using solely the $[Zn(OAc)_4]^{2-}$ DFT model (Fig. S10e–f, ESI†). Since the intermediate concentrations ($n = 5$, 10, 20, and 30) can be fitted well using linear combination of the spectra for most concentrated ($n = 2$) and most diluted ($n = 50$) electrolytes (Fig. S9b–f, ESI†) good fits were obtained using a linear combination of the $[Zn(H_2O)_6]^{2+}$ and $[Zn(OAc)_4]^{2-}$ DFT models (Table S3, ESI† and Fig. 3(e)). The resulting averaged coordination numbers are in

good agreement with the predicted values from MD (Fig. 3(f)). It is important to note, that our experimental and MD simulations data, revealing $[Zn(OAc)_4]^{2-}$ as the main Zn coordination environment for electrolytes with $n < 10$, are in contrast to the previous reports[36] that predicted formation of multiple 6-coordinated complexes including $[Zn(OAc)_6]^{4-}$ as well as the partially hydrated $[Zn(OAc)_3 (H_2O)_2]^-$ for 30 m KOAc + 3 m LiOAc + 3 m ZnOAc$_2$ in water and a Zn^{2+} coordination number > 5.1 oxygens.[36]

Electrochemical characterization

Electrolyte speciation strongly affects reversibility and morphology of Zn plating/stripping as well as parasitic currents associated with processes such as hydrogen evolution. Using cyclic voltammetry (CV), we evaluated effects of electrolyte composition on Zn plating/stripping efficiency at different cut-off plating potentials (−0.1, −0.15 and −0.2 V vs. Zn/Zn^{2+}, see Fig. 4). The CE can be seen following a bell shape with electrolyte concentration for all cut-offs, reaching a maximum of 99.8% (Fig. 4(a)) at intermediate water-to-cation ratios ($n = 10$). This improvement in CE can be attributed to favorable Zn plating kinetics over HER as a result of the change in the Zn^{2+} coordination environment from water-containing to acetate-rich (Fig. 2(C) and Table S3, ESI†).[46] Further increase in concentration leads to the decrease in CE, which can be ascribed to the high stripping overpotentials due to more sluggish ion transport and low conductivities (Table S1 and
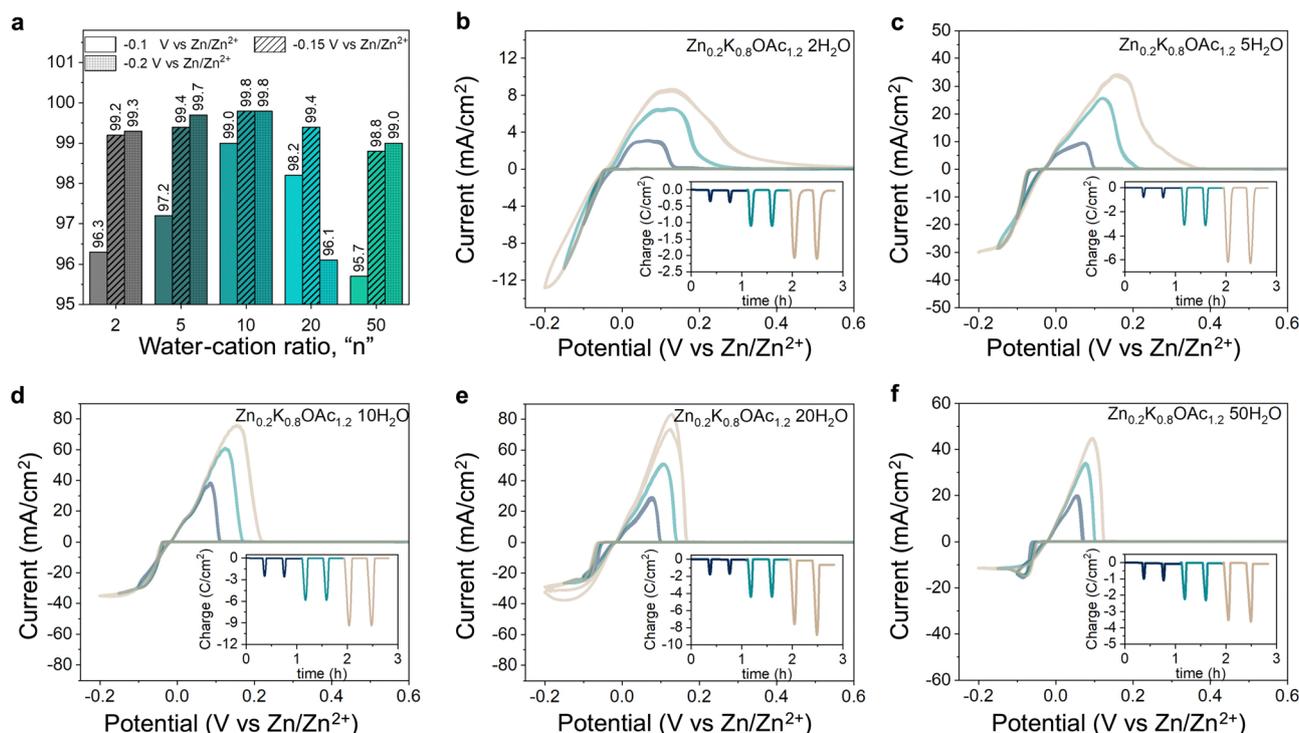

Fig. 4 Cyclic voltammetry profiles collected at 1 mV s^{-1} on Au disk electrodes in Zn–K acetate electrolytes. (a) Averaged Coulombic efficiency as function of water-to-cation ratio "n" for the electrolyte series Zn$_{0.2}$K$_{0.8}$OAc$_{1.2}$ nH$_2$O. CV profiles of Zn plating/stripping at two different cut-off plating voltages (−0.1 and −0.15 V vs. Zn/Zn^{2+}), Insert: Charge vs. time with Coulombic efficiencies per cycle collected in (b) Zn$_{0.2}$K$_{0.8}$OAc$_{1.2}$ 2H$_2$O, (c) Zn$_{0.2}$K$_{0.8}$OAc$_{1.2}$ 5H$_2$O, (d) Zn$_{0.2}$K$_{0.8}$OAc$_{1.2}$ 10H$_2$O, (e) Zn$_{0.2}$K$_{0.8}$OAc$_{1.2}$ 20H$_2$O, (f) Zn$_{0.2}$K$_{0.8}$OAc$_{1.2}$ 50 H$_2$O.

1986 | Energy Environ. Sci., 2023, **16**, 1982–1991
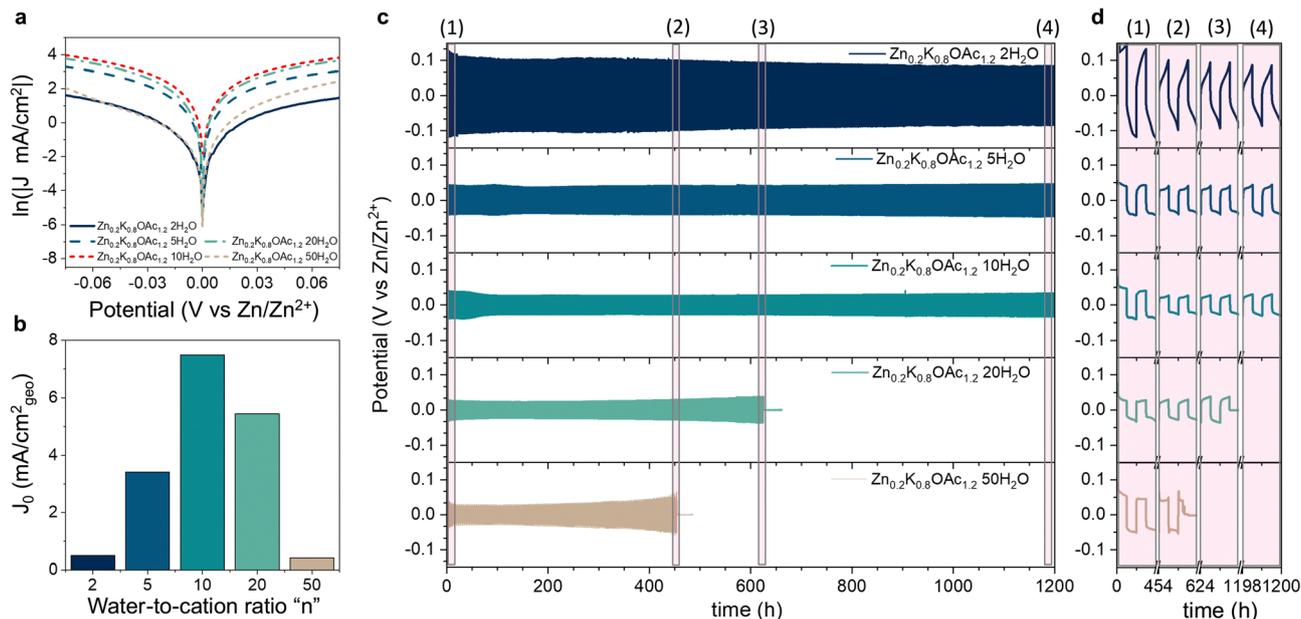
This journal is © The Royal Society of Chemistry 2023

Fig. 5 Electrochemical characterization as function of water–to–cation ratio "n" for the electrolyte series $Zn_{0.2}K_{0.8}OAc_{1.2}$ nH_2O. (a) Tafel plots collected in Zn–K acetate electrolytes. (b) Exchange current density estimated from the Tafel plots. (c) and (d) Galvanostatic cycling of a Zn^0–Zn^0 symmetric cell at 1 mA cm^{-2} and zoom-in of the charging profiles (d). Zoom-ins of GCPL profiles for: (1) t = 0 h: first 2 cycles, (2) t = 454 h: failure of cell with $Zn_{0.2}K_{0.8}OAc_{1.2}$ $50H_2O$ electrolyte, (3) t = 624 h: failure of cell with $Zn_{0.2}K_{0.8}OAc_{1.2}$ $20H_2O$ electrolyte, (4) t = 1289 h: failure of cell with $Zn_{0.2}K_{0.8}OAc_{1.2}$ $10H_2O$ electrolyte, (5) t = 1998 h: last 2 cycles.

Fig. S11, ESI†). Generally, we observed higher CE for higher cut-off potentials (Fig. 4(a)) in agreement with previous reports.[47] The only exception was the electrolyte $Zn_{0.2}K_{0.8}OAc_{1.2}$ $20H_2O$, where the CE drops from 99.4% at −0.15 V to 96.1% at −0.2 V (see Fig. 4(a)), this could be attributed to dendrite formation (and hence electrochemical area increase) as can be seen from higher charge associated with plating during the last CV cycle. Same bell shape CE trend with concentration is observed in a cell configuration with a limited electrolyte amount where the highest CE (99.9%) is obtained in $Zn_{0.2}K_{0.8}OAc_{1.2}$ $10H_2O$ (see Fig. S12, ESI†). Additionally, we characterized CE of Zn plating/stripping using a modified "Aurbach" protocol. The same CE trend was observed with the highest CE (99.1%) for $Zn_{0.2}K_{0.8}OAc_{1.2}$ $10H_2O$ electrolyte (see Fig. S13, ESI†). Further, since DSC results demonstrate a dramatically suppressed freezing point (Fig. 1(c)), for the optimal electrolyte composition ($Zn_{0.2}K_{0.8}OAc_{1.2}$ $10H_2O$) we performed CV plating-stripping at −5 °C and observed similarly high CE of Zn plating/stripping (99.8%) (see Fig. S12a and d and S14, ESI†).

To gain further insights into the effect of electrolyte speciation on the kinetics of Zn plating/stripping process, Tafel slopes were analyzed (Fig. 5(a)) and exchange current density, j_0, values were estimated for each electrolyte (Fig. 5(b) and Fig. S15, ESI†). We observe that the exchange current density reaches its highest value for the intermediate water-to-cation ratio (n = 10). Upon further increase in electrolyte concentration, the exchange current drops considerably to its lowest value at n = 2. It is important to note, that two main factors can affect the exchange current density values: the changes in the reaction constant and the activity of the ions in the solution.

To decouple individual contribution of both factors, the real activity would need to be quantified, which is challenging.[48]

Finally, we performed long-term galvanostatic cycling at 1 mA cm^{-2} of Zn–Zn symmetric cells to assess affinity to dendrite formation as a function of electrolyte speciation. The best cycling stability coupled with low plating/stripping overpotentials is observed for electrolytes at n = 5 and n = 10, where >1000 h of continuous cycling without short-circuiting can be achieved (Fig. 5(c) and (d)). In contrast, cells with electrolytes in the salt-in-water regime (n = 50, n = 20) fail due to dendrite-induced short-circuit after ~450 and 620 h of cycling, respectively. The lower cycling stability may be related to co-presence of Zn^{2+} solvated by water that is known to promote dendritic deposits[49,50] or the formation of stronger concentration gradients and therefore favorable conditions for dendritic growth.[51–53] In electrolytes with the lowest water-to-cation ratio of n = 2 high overpotentials (~200 mV $vs.$ 50 mV for n = 10) were observed due to dramatically increased viscosities and lower ionic conductivities (Fig. 1(b)), resulting in sluggish Zn^{2+} transport (Fig. S11, ESI†). Finally, the cycled Zn electrodes were characterized using SEM revealing a conformal deposit morphology for n = 10, in contrast to rough and flakey deposits observed for n = 50 and n = 2 (Fig. S16, ESI†).

Conclusions

In conclusion, we demonstrate that coordinating anions such as acetate can create a WIS-like coordination environments in electrolytes that are relatively dilute. Using XAS and MD

simulations we show that in a non-concentrated state, the Zn^{2+} coordination environment is already WIS-like, with Zn^{2+} ions being predominantly coordinated by acetate rather than water. These electrolytes can enable Zn plating/stripping with a high CE > 99% and long-term cyclability without a considerable increase in viscosity (which is typical of WIS electrolytes). The best performance is achieved when water-to-cation ratios are 10 and 5 (non-WIS conditions). Overall, we conclude that WIS electrolytes do not always represent an optimal medium for efficient Zn plating/stripping and can result in lower CE and slower kinetics. We suggest that the coordination strength of anion towards Zn is an important parameter in electrolyte engineering determining Zn coordination and plating/stripping efficiency.

Materials and methods

Materials

Zn foil (>99.95%) was purchased from Goodfellow. Zn acetate dihydrate (>99%), Potassium acetate (>99%), and other chemicals were purchased from Sigma Aldrich. The salts were stored and weighed inside the glovebox to avoid water uptake from the atmosphere.

Liquidus line measurements

To obtain liquidus curve depicted in Fig. 1(a), the mixtures of $ZnOAc_2$ and KOAc salts were prepared inside the Ar-filled glovebox and sealed in vials with septa to avoid water uptake from the atmosphere. Water was added to each vial in small increments using a volumetric glass syringe, and the vials were sonicated for ~3 hours at 50 °C after each water addition. After cooling to room temperature, water was added after each heating/sonication process until the salt mixture was entirely dissolved. To ensure that the salts stayed dissolved, the vials were kept at room temperature for at least 7 days.

Conductivity was measured using an Oakton 2700 benchtop meter.

Electrolyte viscosities were measured using an oscillatory rheometer (ARES-G2, TA Instruments). The measurements were performed in the cone-cup and cone-plate (for viscous electrolytes) geometries. The shear rate was variated from 10 to 1000 Hz.

Differential scanning calorimetry (DSC) measurements were carried out using DSC 2500 (TA Instruments). Prior to the measurements, the samples were cycled once from −80 °C to 80 °C and again to −80 °C at a rate of 10 °C min^{-1}. Data was then collected from −80 °C to 80 °C at a rate of 1 °C min^{-1}.

Scanning electron microscopy (SEM)

The SEM images of the cycled electrodes were collected using Hitachi S-4800 microscope.

Nuclear magnetic resonance (NMR)

^{13}C and ^{17}O NMR measurements were acquired on a Bruker ASCEND 400 and 500, respectively. For ^{13}C NMR, 1 mL of each

solution were prepared using D_2O (Sigma Aldrich, 99.9%) to dissolve the respective salt mixtures. The samples were prepared with the same methodology described for the liquidus line (i.e. salts were weighted inside Ar filled glovebox, vials were sealed with septa, D_2O was added using syringe). After preparation, 700 μL of the electrolytes was transferred to NMR tubes (Duran Wheaton Kimble) and tightly closed with a plastic cap and parafilm. For ^{17}O NMR measurement, 700 μL of the respective electrolytes $Zn_{0.2}K_{0.8}OAc_{1.2}$ nH_2O were transferred to NMR tubes, to improve ^{17}O signal, 10 μL of 7.7% ^{17}O enriched H_2O (Sigma Aldrich) was added to each sample. The samples were measured at 25 ± 0.1 °C. The collected data was processed using MestReNova X64.

X-Ray absorption spectroscopy (XAS)

XAS was measured in the Swiss Light source at PSI in the Line X10DA-SuperXAS using a Si (111) monochromator and an ionization chamber for transmission detection. The XAS collection was done in Quick EXAFS (QEXAFS) mode[54] around the Zn K-edge (9450–10 800 eV), using Zn metal foil for energy calibration (Edge at 9659 eV). To avoid beam damage, during measurement the electrolyte was pumped at a rate of 100 μL min^{-1} through a microfluidic channel from TOPAS (ChipShop, Germany) with a channel depth of 400 μm. The data was collected for 5 minutes and processed using the ProXAS GUI[55] (averaging of QEXAFS collected data, calibration) and the Demeter software package[56] (post processing, and fitting). The XAS data processing was done in Athena, edge energy was defined as the energy at which the 2nd derivate is zero. The EXAFS data were extracted from normalized XAS spectra and by fitting a spline to the data region between k = 3–12 Å^{-1}. The resulting EXAFS data sets were then plotted using a k^3 weighting. For the fitting, the amplitude reduction factor S_0^2 was assumed to be unity based on prior literature.[57]

Total X-ray scattering

Total X-ray scattering was acquired at the Advanced Photon Source (APS) at Argonne National Laboratory (ANL) at beamline 11-ID-B with an X-ray Energy of 58.66 keV (λ = 0.213 Å). A PerkinElmer XRD 1621 detector was placed at a distance of 0.296 m from the sample. The data ranged from q = 0.26–17 Å^{-1}, corresponding to length scales of 24 Å and 0.37 Å, respectively. Samples were filled into 2 mm quartz X-ray capillaries with a wall thickness of 0.01 mm (WJM-Glass) and sealed with Master Bond EP 30-2 low outgassing epoxy resin. Data were recorded for a total of 690 s on a total of 3 different positions on the capillary.

Data with $q \gtrsim 2$ Å^{-1} originates in inter- and intra-molecular correlations, which are also represented in the real space pair distribution (PDF). In contrast, data with $q \lesssim 2$ Å^{-1} corresponds to scattering originating from longer length scales such as nanoscale phase segregation in the form of ion clusters.[43] The data reduction and analysis were performed using PyFAI and PDFGetX2[58,59] to extract $S(q)$ and PDF in $G(r)$ space. The background was subtracted and scaled with the sample transmission. We corrected our data for standard geometric detector corrections, polarization, sample self-absorption,

oblique incidence, and Compton scattering. A Lorch function was applied before the Fourier transformation to reduce termination ripples.

Electrochemical characterization

CV plating/stripping was performed in a 3-electrode cell using a 2 mm Au disk working electrode (CH Instruments) and a Zn foil as counter, and a separate Zn foil as reference electrodes. Additional experiments were performed using a Swagelok cell in a 3-electrode configuration, where 2 mm Au disk served as working electrode, 6 mm Zn disk as counter electrode, additional Zn foil was used as reference. Electrolyte volume was kept at 150 μL and working and counter electrodes were separated using a 380 μm Teflon spacer. To collect CVs at -5 °C, electrochemical cell was placed into Binder KB 53 environmental chamber with temperature set at -5 °C.

The modified Aurbach protocol was performed using 2 electrode Swagelok cell with Cu disk working electrode ($\varnothing$ 12.5 mm) and Zn foil disk counter electrode, glass fiber was used as a separator, 100 μl of electrolyte was added during assembly. The detailed experimental sequence was the following: first, plating, stripping and re-deposition of excess amount of Zn was performed with a current density of 3 mA cm^{-2} and a specific areal capacity of 5 mA h cm^{-2}, second Zn stripping and plating sequences were performed for 10 times with a current density of 0.5 mA cm^{-2} and a specific areal capacity of 1 mA h cm^{-2}. Finally, Zn stripping was carried out with current density of 3 mA cm^{-2} with a cut off voltage set at 0.5 V.

To reduce effect of mass transfer limitations, exchange current measurements were performed using rotating disk electrode (RDE) set-up at 2000 rpm. The working electrode was a 4 mm Au disk with electrodeposited layer of Zn that was polished with 300 nm alumina powder (CH instruments) and cleaned and sonicated in Milli-Q water before the experiment. The counter electrode was a Zn foil placed at $\sim$5 mm from the working electrode, the reference electrode was Ag/AgCl in 1M KCl (CH instruments). The linear fitting of the Tafel slopes was done in the negative overpotential range from -25 to -50 mV (Fig. S13, ESI†).

Zn–Zn symmetric cells cycling test was performed in 2-electrode Swagelok cell with Zn foil disk electrodes (6 mm in diameter), a 1 mm thick glass fiber separator ($\sim$0.5 mm after compression) and 75 μL of electrolyte. The cells were aged for 1 day and afterwards were cycled in a constant current program at 1 mA cm^{-2} for a specific areal capacity of 0.5 mA h cm^{-2} (30 min). The cut off voltages were fixed at $\pm$0.5 V.

Molecular dynamics simulations – density functional theory calculations

Molecular dynamics simulations using the AMOEBA polarizable force field were performed using a locally-modified version of Tinker HP v1.2 to output the stress tensor at the desired frequency.[60,61] Two parameterizations of the force field were considered, the first of which (force field 1, FF1) produced results that compared favorably against experimental conductivity data (Table S1, ESI†) and a second (force field 2, FF2)

which lowered the average error in the binding energies between the force field prediction and density functional theory with an assortment of solvate species composed of K$^+$ or Zn^{2+} with differing amounts of OAc$^-$ and water. Due to FF2 systematically overestimating conductivities, the analysis presented here focuses on results extracted from simulations with FF1. A detailed discussion of the workflow for the simulation and analysis methodologies is expanded upon in the ESI.†

Conflicts of interest

There are no conflicts to declare.

Acknowledgements

References

1 J. P. Barton and D. G. Infield, *IEEE Trans. Energy Convers*, 2004, **19**, 441–448.

2 T. M. Gür, *Energy Environ. Sci.*, 2018, **11**, 2696–2767.

3 D.-S. Kourkoumpas, G. Benekos, N. Nikolopoulos, S. Karellas, P. Grammelis and E. Kakaras, *Appl. Energy*, 2018, **231**, 380–398.

4 A. Mamen and U. Supatti, 2017.

5 Z. Yang, J. Zhang, M. C. W. Kintner-Meyer, X. Lu, D. Choi, J. P. Lemmon and J. Liu, *Chem. Rev.*, 2011, **111**, 3577–3613.

6 C. Curry, 2017.

7 Y. Tian, G. Zeng, A. Rutt, T. Shi, H. Kim, J. Wang, J. Koettgen, Y. Sun, B. Ouyang, T. Chen, Z. Lun, Z. Rong, K. Persson and G. Ceder, *Chem. Rev.*, 2021, **121**, 1623–1669.

8 J. Zhang, X. Yao, R. K. Misra, Q. Cai and Y. Zhao, *J. Mater. Sci. Technol.*, 2020, **44**, 237–257.

9 H. Wang, R. Tan, Z. Yang, Y. Feng, X. Duan and J. Ma, *Adv. Energy Mater.*, 2021, **11**, 2000962.

This journal is © The Royal Society of Chemistry 2023

Energy Environ. Sci., 2023, **16**, 1982–1991 | **1989**

10 H. Jia, Z. Wang, B. Tawiah, Y. Wang, C.-Y. Chan, B. Fei and F. Pan, *Nano Energy*, 2020, **70**, 104523.

11 K. Hu, X. Guan, R. Lv, G. Li, Z. Hu, L. Ren, A. Wang, X. Liu and J. Luo, *Chem. Eng. J.*, 2020, **396**, 125363.

12 M. Kaya, S. Hussaini and S. Kursunoglu, *Hydrometallurgy*, 2020, **195**, 105362.

13 M. B. Lim, T. N. Lambert and B. R. Chalamala, *Mater. Sci. Eng. R Rep.*, 2021, **143**, 100593.

14 W. Lu, C. Zhang, H. Zhang and X. Li, *ACS Energy Lett.*, 2021, **6**, 2765–2785.

15 V. Verma, S. Kumar, W. Manalastas and M. Srinivasan, *ACS Energy Lett.*, 2021, **6**, 1773–1785.

16 X. Guo, Z. Zhang, J. Li, N. Luo, G.-L. Chai, T. S. Miller, F. Lai, P. Shearing, D. J. L. Brett, D. Han, Z. Weng, G. He and I. P. Parkin, *ACS Energy Lett.*, 2021, **6**, 395–403.

17 Q. Zhang, J. Luan, Y. Tang, X. Ji and H. Wang, *Angew. Chem., Int. Ed.*, 2020, **59**, 13180–13191.

18 L. Ma, M. A. Schroeder, T. P. Pollard, O. Borodin, M. S. Ding, R. Sun, L. Cao, J. Ho, D. R. Baker, C. Wang and K. Xu, *Energy Environ. Mater.*, 2020, **3**, 516–521.

19 L. Cao, D. Li, T. Pollard, T. Deng, B. Zhang, C. Yang, L. Chen, J. Vatamanu, E. Hu, M. J. Hourwitz, L. Ma, M. Ding, Q. Li, S. Hou, K. Gaskell, J. T. Fourkas, X.-Q. Yang, K. Xu, O. Borodin and C. Wang, *Nat. Nanotechnol.*, 2021, **16**, 902–910.

20 M. Yan, N. Dong, X. Zhao, Y. Sun and H. Pan, *ACS Energy Lett.*, 2021, 3236–3243, DOI: **10.1021/acsenergylett.1c01418**.

21 Y. Zhang, G. Wan, N. H. C. Lewis, J. Mars, S. E. Bone, H.-G. Steinrück, M. R. Lukatskaya, N. J. Weadock, M. Bajdich, O. Borodin, A. Tokmakoff, M. F. Toney and E. J. Maginn, *ACS Energy Lett.*, 2021, **6**, 3458–3463.

22 F. Wang, O. Borodin, T. Gao, X. Fan, W. Sun, F. Han, A. Faraone, J. A. Dura, K. Xu and C. Wang, *Nat. Mater.*, 2018, **17**, 543–549.

23 T. F. Burton, R. Jommongkol, Y. Zhu, S. Deebansok, K. Chitbankluai, J. Deng and O. Fontaine, *Curr. Opin. Electrochem.*, 2022, **35**, 101070.

24 V. A. Azov, K. S. Egorova, M. M. Seitkalieva, A. S. Kashin and V. P. Ananikov, *Chem. Soc. Rev.*, 2018, **47**, 1250–1284.

25 S. B. Pillai, R. J. Wilcox, B. G. Hillis, B. P. Losey and J. D. Martin, *J. Phys. Chem. B*, 2022, **126**, 2265–2278.

26 W. Yang, Y. Yang, H. Yang and H. Zhou, *ACS Energy Lett.*, 2022, **7**, 2515–2530.

27 A. Bayaguud, Y. Fu and C. Zhu, *J. Energy Chem.*, 2022, **64**, 246–262.

28 J. Han, A. Mariani, A. Varzi and S. Passerini, *J. Power Sources*, 2021, **485**, 229329.

29 W. Sun, F. Wang, B. Zhang, M. Zhang, V. Küpers, X. Ji, C. Theile, P. Bieker, K. Xu, C. Wang and M. Winter, *Science*, 2021, **371**, 46.

30 S. Alvarez, *Chem. – Eur. J.*, 2020, **26**, 4350–4377.

31 J. Jorne and W. T. Ho, *J. Electrochem. Soc.*, 1982, **129**, 907–912.

32 X. Wu, Y. Xu, C. Zhang, D. P. Leonard, A. Markir, J. Lu and X. Ji, *J. Am. Chem. Soc.*, 2019, **141**, 6338–6344.

33 M. R. Lukatskaya, J. I. Feldblyum, D. G. Mackanic, F. Lissel, D. L. Michels, Y. Cui and Z. Bao, *Energy Environ. Sci.*, 2018, **11**, 2876–2883.

34 J. Han, A. Mariani, M. Zarrabeitia, Z. Jusys, R. J. Behm, A. Varzi and S. Passerini, *Small*, 2022, **18**, 2201563.

35 P. L. Stigliano, N. Pianta, S. Bonizzoni, M. Mauri, R. Simonutti, R. Lorenzi, B. Vigani, V. Berbenni, S. Rossi, P. Mustarelli and R. Ruffo, *Phys. Chem. Chem. Phys.*, 2021, **23**, 1139–1145.

36 J. Han, A. Mariani, A. Varzi and S. Passerini, *J. Power Sources*, 2021, **485**, 229329.

37 C. Austen Angell, Y. Ansari and Z. Zhao, *Faraday Discuss.*, 2012, **154**, 9–27.

38 Q. Zhang, Y. Ma, Y. Lu, L. Li, F. Wan, K. Zhang and J. Chen, *Nat. Commun.*, 2020, **11**, 4463.

39 J. Holoubek, H. Liu, Z. Wu, Y. Yin, X. Xing, G. Cai, S. Yu, H. Zhou, T. A. Pascal, Z. Chen and P. Liu, *Nat. Energy*, 2021, **6**, 303–313.

40 T. Sun, X. Yuan, K. Wang, S. Zheng, J. Shi, Q. Zhang, W. Cai, J. Liang and Z. Tao, *J. Mater. Chem. A*, 2021, **9**, 7042–7047.

41 Q. Zhang, K. Xia, Y. Ma, Y. Lu, L. Li, J. Liang, S. Chou and J. Chen, *ACS Energy Lett.*, 2021, **6**, 2704–2712.

42 Y. Zhu, J. Yin, X. Zheng, A.-H. Emwas, Y. Lei, O. F. Mohammed, Y. Cui and H. N. Alshareef, *Energy Environ. Sci.*, 2021, **14**, 4463–4473.

43 H. V. R. Annapureddy, H. K. Kashyap, P. M. De Biase and C. J. Margulis, *J. Phys. Chem. B*, 2011, **115**, 9507–9508.

44 W. Linert, Y. Fukuda and A. Camard, *Coord. Chem. Rev.*, 2001, **218**, 113–152.

45 I. P. Oliveri and S. Di Bella, *Dalton Trans.*, 2017, **46**, 11608–11614.

46 J. Cao, D. Zhang, X. Zhang, Z. Zeng, J. Qin and Y. Huang, *Energy Environ. Sci.*, 2022, **15**, 499–528.

47 L. Ma, M. A. Schroeder, O. Borodin, T. P. Pollard, M. S. Ding, C. Wang and K. Xu, *Nat. Energy*, 2020, **5**, 743–749.

48 A. J. Bard and L. R. Faulkner, *Electrochemical Methods: Fundamentals and Applications*, Wiley, 2nd edn, 2001.

49 P. Sun, L. Ma, W. Zhou, M. Qiu, Z. Wang, D. Chao and W. Mai, *Angew. Chem., Int. Ed.*, 2021, **60**, 18247–18255.

50 Z. Cao, P. Zhuang, X. Zhang, M. Ye, J. Shen and P. M. Ajayan, *Adv. Energy Mater.*, 2020, **10**, 2001599.

51 Y. Zuo, K. Wang, P. Pei, M. Wei, X. Liu, Y. Xiao and P. Zhang, *Mater. Today Energy*, 2021, **20**, 100692.

52 K. Wang, P. Pei, Z. Ma, H. Chen, H. Xu, D. Chen and X. Wang, *J. Mater. Chem. A*, 2015, **3**, 22648–22655.

53 C. Brissot, M. Rosso, J. N. Chazalviel and S. Lascaud, *J. Power Sources*, 1999, **81–82**, 925–929.

54 O. Muller, M. Nachtegaal, J. Just, D. Lutzenkirchen-Hecht and R. Frahm, *J. Synchrotron Radiat.*, 2016, **23**, 260–266.

55 A. H. Clark, J. Imbao, R. Frahm and M. Nachtegaal, *J. Synchrotron Radiat.*, 2020, **27**, 551–557.

56 B. Ravel and M. Newville, *J. Synchrotron Radiat.*, 2005, **12**, 537–541.

57 P. D'Angelo, V. Barone, G. Chillemi, N. Sanna, W. Meyer-Klaucke and N. V. Pavel, *J. Am. Chem. Soc.*, 2002, **124**, 1958–1967.

58 X. Qiu, J. W. Thompson and S. J. L. Billinge, *J. Appl. Crystallogr.*, 2004, **37**, 678.

59 G. Ashiotis, A. Deschildre, Z. Nawaz, J. P. Wright, D. Karkoulis, F. E. Picca and J. Kieffer, *J. Appl. Crystallogr.*, 2015, **48**, 510–519.

1990 | *Energy Environ. Sci.*, 2023, **16**, 1982–1991

This journal is © The Royal Society of Chemistry 2023

60 J. W. Ponder, C. Wu, P. Ren, V. S. Pande, J. D. Chodera, M. J. Schnieders, I. Haque, D. L. Mobley, D. S. Lambrecht and R. A. DiStasio Jr, *J. Phys. Chem. B*, 2010, **114**, 2549–2564.

61 L. Lagardère, L.-H. Jolly, F. Lipparini, F. Aviat, B. Stamm, Z. F. Jing, M. Harger, H. Torabifard, G. A. Cisneros, M. J. Schnieders, N. Gresh, Y. Maday, P. Y. Ren, J. W. Ponder and J.-P. Piquemal, *Chem. Sci.*, 2018, **9**, 956–972.

This journal is © The Royal Society of Chemistry 2023

Energy Environ. Sci., 2023, **16**, 1982–1991 | **1991**